



HAL
open science

Sun glitter imagery of surface waves. Part 2: Waves transformation on ocean currents

Vladimir Kudryavtsev, Maria Yurovskaya, Bertrand Chapron, Fabrice Collard,
Craig Donlon

► **To cite this version:**

Vladimir Kudryavtsev, Maria Yurovskaya, Bertrand Chapron, Fabrice Collard, Craig Donlon. Sun glitter imagery of surface waves. Part 2: Waves transformation on ocean currents. *Journal of Geophysical Research. Oceans*, 2017, 122 (2), pp.1384-1399. <10.1002/2016JC012426>. <hal-04201860>

HAL Id: hal-04201860

<https://hal.science/hal-04201860v1>

Submitted on 15 Sep 2023

HAL is a multi-disciplinary open access archive for the deposit and dissemination of scientific research documents, whether they are published or not. The documents may come from teaching and research institutions in France or abroad, or from public or private research centers.

L'archive ouverte pluridisciplinaire **HAL**, est destinée au dépôt et à la diffusion de documents scientifiques de niveau recherche, publiés ou non, émanant des établissements d'enseignement et de recherche français ou étrangers, des laboratoires publics ou privés.



Copyright - All rights reserved

RESEARCH ARTICLE

10.1002/2016JC012426

This article is a companion to
Kudryavtsev et al. [2017],
doi:10.1002/2016JC012425.

Key Points:

- Satellite Sun Glitter Imagery (SSGI) provides unique opportunities to study ocean wave refraction on surface currents
- As demonstrated, Grand Agulhas current, reconstructed from satellite altimetry, can significantly deflect in-coming swell systems
- Ray-tracing calculations and SSGI unambiguously reveal the wave-trapping phenomenon leading to strong enhancement of swell energy

Correspondence to:

V. Kudryavtsev,
kudr@rshu.ru

Citation:

Kudryavtsev, V., M. Yurovskaya, B. Chapron, F. Collard, and C. Donlon (2017), Sun glitter imagery of surface waves. Part 2: Waves transformation on ocean currents, *J. Geophys. Res. Oceans*, 122, 1384–1399, doi:10.1002/2016JC012426.

Received 5 OCT 2016

Accepted 19 JAN 2017

Accepted article online 31 JAN 2017

Published online 20 FEB 2017

© 2017. American Geophysical Union.
All Rights Reserved.

Sun glitter imagery of surface waves. Part 2: Waves transformation on ocean currents

Vladimir Kudryavtsev^{1,2} , Maria Yurovskaya² , Bertrand Chapron³, Fabrice Collard⁴, and Craig Donlon⁵

¹Russian State Hydrometeorological University, St. Petersburg, Russia, ²Marine Hydrophysical Institute RAS, Sebastopol, Russia, ³Institute Francais de Recherche pour l'Exploitation de la Mer, Plouzané, France, ⁴OceanDataLaboratory, Brest, France, ⁵European Space Agency, ESA/ESTEC, Noordwijk, Netherlands

Abstract Under favorable imaging conditions, the Sentinel-2 Multi-Spectral Instrument (MSI) can provide spectacular and novel quantitative ocean surface wave directional measurements in satellite Sun Glitter Imagery (SSGI). Owing to a relatively large-swath with high-spatial resolution (10 m), ocean surface roughness mapping capabilities, changes in ocean wave energy, and propagation direction can be precisely quantified at very high resolution, across spatial distances of 10 km and more. This provides unique opportunities to study ocean wave refraction induced by spatial varying surface currents. As expected and demonstrated over the Grand Agulhas current area, the mesoscale variability of near-surface currents, documented and reconstructed from satellite altimetry, can significantly deflect in-coming south-western swell systems. Based on ray-tracing calculations, and unambiguously revealed from the analysis of Sentinel-2 MSI SSGI measurements, the variability of the near-surface current explains significant wave-current refraction, leading to wave-trapping phenomenon and strong local enhancement of the total wave energy. In addition to its importance for wave modeling and hazard prediction, these results open new possibilities to combine different satellite measurements and greatly improve the determination of the upper ocean mesoscale vorticity motions.

1. Introduction

In Part 1, a method is described to retrieve directional spectra of the surface wave elevations using Satellite Sun Glitter Imagery (SSGI). Applied to Sentinel-2 Multi-Spectral Instrument (MSI) measurements, the unique instrumentation and configuration of multichannel offset detectors can be used to derive 2-D directional wave spectra for wavelength range $\lambda > 20$ m, as well as to also assess the local dispersion relation.

In this companion paper, we further exploit the high-resolution space-time capability of large-swath Sentinel-2 MSI SSGI to quantitatively map the transformation of the dominant surface waves, swell and wind-driven spectral peak waves, by ocean surface currents. Deflected and trapped wave packets can lead to the unexpected occurrence of abnormally high surface waves, over areas where local winds and waves should be fairly ordinary [Mallory, 1974; Rapizo et al., 2014; see also Lavrenov, 2003, for review].

In the Great Agulhas current region, wave packet trapping effects are generally considered to be the most plausible mechanism for the appearance of abnormally high swells [Gutshabash and Lavrenov, 1986]. Extracting spectra from SAR SIR-B measurements, Irvine and Tilley [1988] reported the dramatic swell energy intensification over the Great Agulhas current region. Kudryavtsev et al. [1995] also reported results of field measurements of wind-driven trapped waves in the Gulf Stream, with measurable significant amplification of the energy of wind-driven seas opposing the current.

More generally, apart from spectacular and specific cases of wave-trapping enhancement, the interaction of deep water waves with spatially varying ocean currents had been investigated and reported in earlier studies using satellite SAR measurements [see e.g., Meadows et al., 1983, McLeish and Ross, 1985, Mapp et al., 1985]. Efficiency of SAR to detect ocean current had been further exploited in terms of conversion of observed wave refraction to estimate the surface current parameters [Barnett et al., 1989; Liu et al., 1994].

Over the Great Agulhas current area, the larger-scale mesoscale variability of the near-surface currents can efficiently be reconstructed from satellite altimetry [Rouault et al., 2010], to help wave ray-tracing

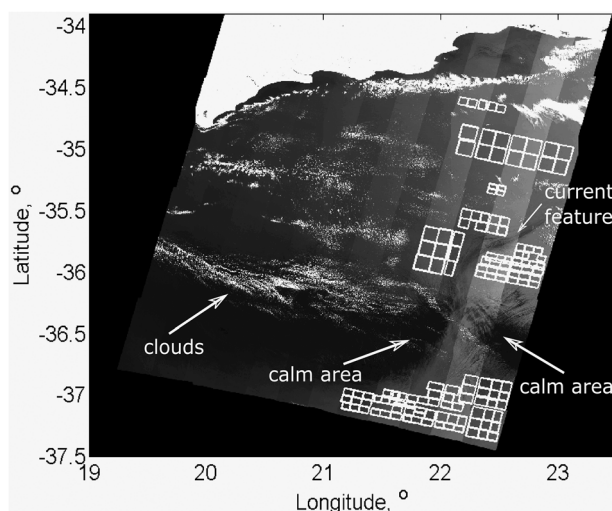


Figure 1. Two Sentinel-2 MSI images #S2A_OPER_PRD_MSIL1C_PDMC 20160104T172441_R078_V20160104T084040_20160104T084040 and #S2A_OPER_PRD_MSIL1C_PDMC 20160104T172409_R078_V20160104T084040_20160104T084040 over the Great Agulhas current region, 4 January 2016. White frames indicate selected fragments used for our wave processing. White arrows indicate (i) a calm area over which the sun glitter is “eroded” corresponding to low roughness MSS values, and (ii) a current feature over which roughness MSS is decreased due to either current convergence with accumulated surfactants acting to suppress short-scale waves, or current divergence with local lower SST, leading, as a consequence, to increase the atmospheric stratification and to decrease the surface wind stress and the roughness MSS. Image contains modified Copernicus data (2016).

calculations. In section 1, we describe the study area and the satellite data employed. Section 2 provides description of the data processing. As selected, a fragment of a sun glitter Sentinel-2 strip exhibits significant changes of the surface wave characteristics. These changes occur over a rather short spatial scale, of order 10 km. In section 3, the Sentinel-2 data analysis of surface wave transformation is given. It clearly demonstrates the strong enhancement of swell energy caused by refraction, and related local dispersion relationship changes as derived from Sentinel-2 MSI spatiotemporal measurements. The current-induced variability thus creates gradients in wave heights that would be difficult to observe without high-resolution wide swath SSGI. Model simulations are given in section 4, and a summary of the obtained results is given section 5.

2. Study Area and Data

On 4 January 2016, Sentinel-2 MSI images were acquired over the Great Agulhas

Current region. The red channel B04 (665 nm) output is shown in Figure 1. As obtained, the SSGI is partitioned between “bright-and-dark” stripes, originating from the specific configuration of Sentinel-2 optical detectors. As discussed in Part 1, this feature of the MSI design is essential to determine 2-D surface brightness gradients and thus to recover 2-D spectra of the surface wave elevations. The image further exhibits some very calm wind areas resulting in an “erosion” of the sun glitter reflections. A dark linear feature is clearly visible in the image that is a likely manifestation of the ocean current impact on short-scale surface waves in the wavelength range of order 10 m and shorter [Kudryavtsev et al., 2012; Rasche et al., 2014]. This

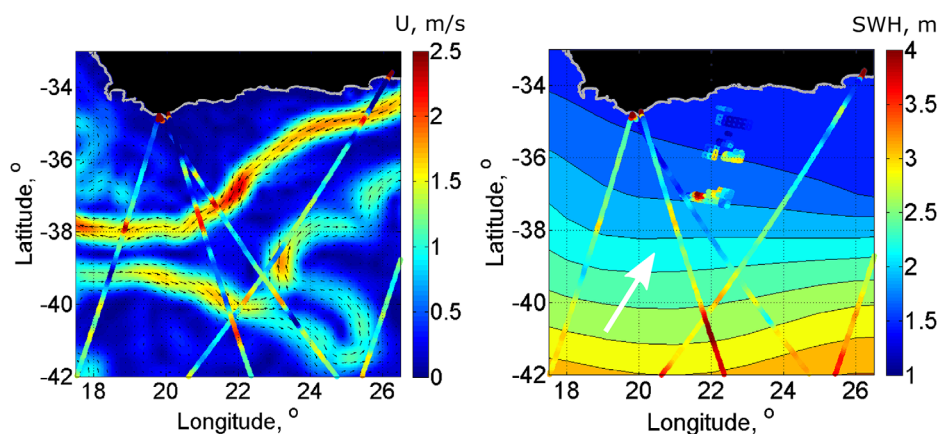


Figure 2. (left) Geostrophic surface current velocity corresponding to 4 January 2016, <http://www.aviso.altimetry.fr/en/data/products/sea-surface-height-products/global/madt-h-uv.html>, and SWH anomalies, $(H_s - \bar{H}_s) / \bar{H}_s$ (in conventional units), along the altimeter track, where \bar{H}_s corresponds to a 250 km moving window along the altimeter track. (right) Mean field of SWH on the same date from <ftp://ftp.aviso.oceanobs.com/pub/oceano/AVISO/wind-wave/nrt/mswh/merged>, altimeter tracks (Jason-2 and AltiKa Saral on 3–5 January 2016) taken from <ftp://avisoftp.cnes.fr/AVISO/pub>, and SWH (color patches) derived from S2 MSI imagettes. The white arrow in the plot indicates the mean swell direction on 4 January 2016.

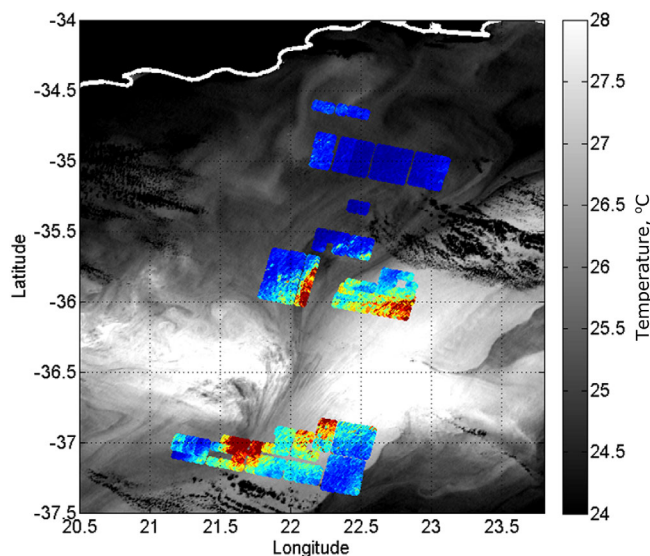


Figure 3. Sea surface temperature (SST) field, 4 January 2016, 12:20 GMT obtained from VIIRS, ftp://podaac-www.jpl.nasa.gov/OceanTemperature/ghrsst/data/GDS2/L2P/VIIRS_NPP/OSPO/v2.4/2016/004/20160104122000-OSPO-L2P_GHRSSST-SSTskin-VIIRS_NPP-ACSP0_V2.40-v02.0-fv01.0.nc. Overlaid, color-coded wave energy derived from S2 MSI imagettes. Image contains modified Copernicus data (2016).

upper ocean feature may be associated with surface current divergence and accompanied with local changes in sea surface temperature (SST) to locally increase the atmospheric stratification, consequently lowering the surface wind stress and surface roughness [Beal et al., 1997; Kudryavtsev et al., 1996, 2005; Kozlov et al., 2012].

The Sentinel-2 MSI measurements are further complemented by satellite altimeter measurements, from which ocean geostrophic current and significant wave height estimates can be made as shown in Figure 2. As mapped, the altimeter-derived currents exhibit intense mesoscale variability with surface velocities reaching 2 m/s, in the Agulhas core current (Figure 2, left). The derived mean field of the significant wave height (SWH), Figure 2 (right) displays a general decrease from the South to the North. Around the

acquisition date, waves entering the Agulhas region were generated from the southern high-wind ocean areas, traveling in a north-easterly direction.

Individual altimeter-track measurements have been overlaid on to the mean SWH field (Figure 2, right) and exhibit large local SWH deviations. Anomalies, $H_s - \bar{H}_s$, scaled by mean values, \bar{H}_s , Figure 2 left, are derived from an along-track 250 km moving average, display some remarkable features. In particular, some local enhancements can be spatially associated to the current “jet.” Yet, other SWH anomalies are not visually linked to the local current, and may well express nonlocal swell-current interactions with SWH enhanced along the swell trajectories [Rapizo et al., 2014].

The sea surface temperature (SST) field shown in Figure 3 generally traces the Agulhas current. A marked step-like SST change marks the south boundary. Around -36.5 latitude, a warm SST area coincides with the calm glitter area shown in Figure 1. It likely originates from a solar heating of the subsurface upper ocean layer, known as afternoon effect that creates a diurnal thermocline in calm areas of the sea surface and then masks the manifestation of the Agulhas current in the SST field [see e.g., Kudryavtsev and Soloviev, 1990; Stuart-Menteth et al., 2005, for more details and application to remote sensing].

3. Data Processing

To perform surface wave analysis, the Sentinel-2 MSI SSGI is first subdivided into imagettes, as indicated in Figure 1. It is dictated by the necessity to avoid the impact of spatial MSS anomalies caused by the presence of clouds, wind variability, i.e., the calm area, or by the current, i.e., the linear dark features visible in Figure 1.

Over the selected imagettes, the processing follows the procedure described in Part 1, and illustrated in Figures 4a and 4b. Brightness variations, \tilde{B} , are converted to the surface elevation field following equation (17) from Part 1, with the components of the brightness gradient directly derived from the mean shape of the SSGI distributions. Figure 4c shows the reconstructed field of surface elevations, and Figure 4d shows field of wave energy (variance of surface elevations) revealing its strong spatial variability. A 3-D zoom of the surface elevation field shown in Figure 4c is presented in Figure 5. Two transects are shown in Figure 6 corresponding to the surface elevations in areas with lower and higher wave energy of Figure 4d. The surface elevation profile corresponding to the more energetic part of the image exhibits wave group-structure,

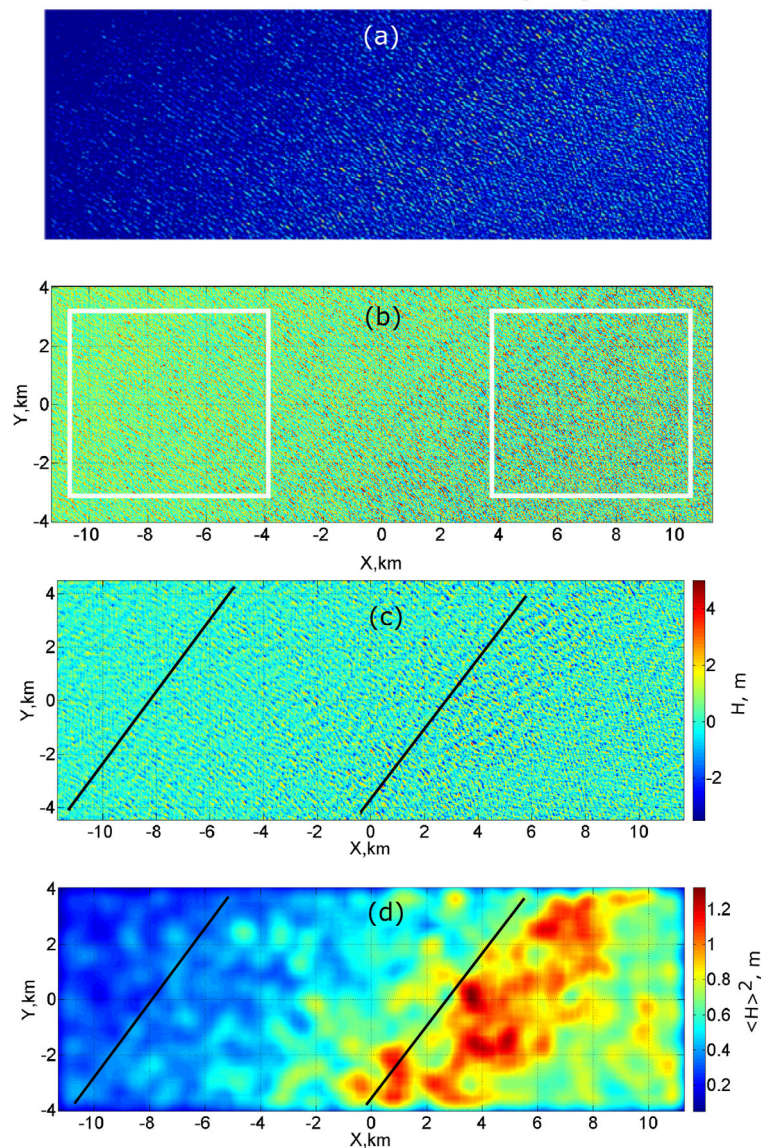


Figure 4. (a) Fragment of original S2 MSI image, location correspond to frames 27–28–29 reported Figure 9; (b) SSGI brightness variations; (c) surface elevations reconstructed from the brightness variations using (17) with (15) in Part 1; (d) estimated variance field of the sea surface elevations (wave energy). Image contains modified Copernicus data (2016).

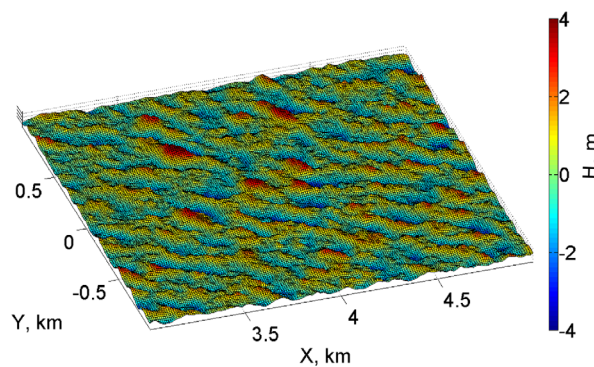


Figure 5. Zoom of the Sentinel-2 MSI SSGI derived surface elevation field shown in Figure 4c.

with some wave overshoots, demonstrating the possible random occurrence of very high “individual” waves. SSGI brightness variations spectra, $S_b(\mathbf{K})$, and corresponding surface wave elevation spectra, $S_\zeta(\mathbf{K})$, using equation (18) from Part 1, are shown in Figure 7. As obtained, brightness and wave elevation spectra derived in the left and right side of the image (white squares in Figure 4b) are very different, both in terms of shape and

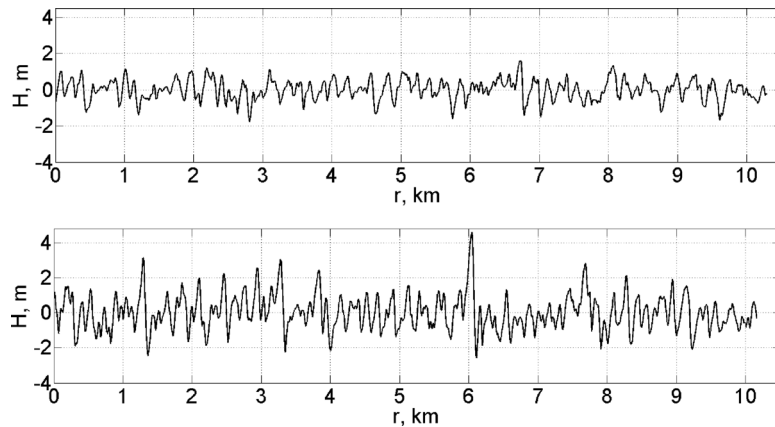


Figure 6. Ocean surface elevation profiles along the (top) left transect and (bottom) right transect shown Figure 4c.

spectral level. In particular, the wave spectrum corresponding to the enhanced wave energy area, displays a broad angular distribution. This is likely related to the appearance of an additional wave system.

As discussed in Part 1, the time delay between the Sentinel-2 two channels (B04 (665 nm) and B08 (842 nm)) measurements can efficiently help to remove the wave propagation ambiguity. Such a procedure, based on a cross-spectral analysis, has been applied to the elevation spectra in Figure 7. Moreover, the

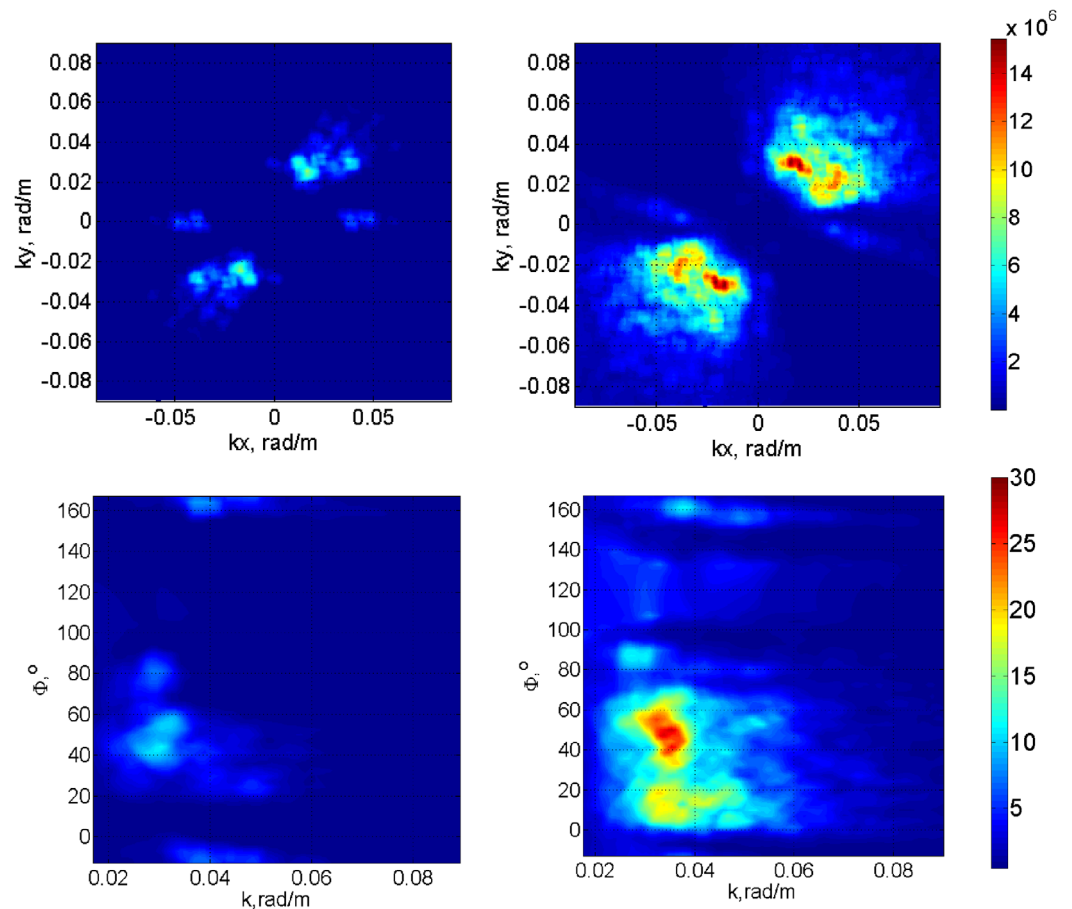


Figure 7. (top row) Wave number spectra of the SSGI brightness variations of the area enclosed in the left and right squares indicated in Figure 4b, respectively. (bottom row) Directional spectra of surface elevations derived from the brightness spectra using equations (18) and (15) from Part 1.

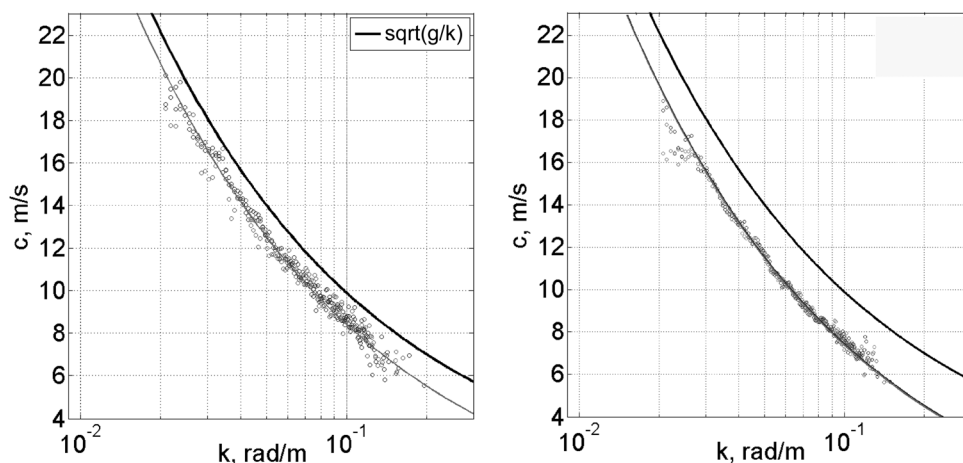


Figure 8. Phase shift between channels B04 (665 nm) and B08 (842 nm) compared to linear dispersion relation $c=c(k)$ for the left and right frames, indicated in Figure 4b. Symbols are estimates for different directions fitted by gray line; the black solid line corresponds to the linear model dispersion relation, $c=(g/k)^{1/2}$

cross-spectral analysis (see section 3.3. in Part 1 for details) helps to measure the dispersion relation of the surface waves and to assess the wave number-dependent Doppler shifts caused by the ocean current, as illustrated in Figure 8 for the left and right inserts indicated in Figure 4b. In both cases, the dispersion relation remarkably deviates from the expected linear relation. As interpreted, the overall Doppler shift will trace the ocean surface current. The shift is stronger for the right-hand frame indicating a larger current velocity that coincides with strong wave energy enhancement.

4. Observations of Mesoscale Wave Transformation

From reconstructed surface elevations for each of the selected frames in Figure 1, a wave energy field can be estimated, and overlaid on the SST field of Figure 3. The resulting field of SWH is overlaid on the altimeter data in Figure 2 (right). North of the Agulhas current, the Sentinel-2 SSGI derived SWHs are spatially relatively uniform, with values consistent with the altimeter data (Figure 2, right). In the area of surface current, SWHs from both Sentinel-2 SSGI and the different altimeters exhibit large spatial variability. Altimeter SWH anomalies (Figure 2, left) reveal a correlation with the local currents: wave heights increase (respectively, decrease) for swell traveling against (respectively, along) the current. This is confirmed by the spatial distribution of the wave energy field derived from the SSGI overlaid on the SST field in Figure 3.

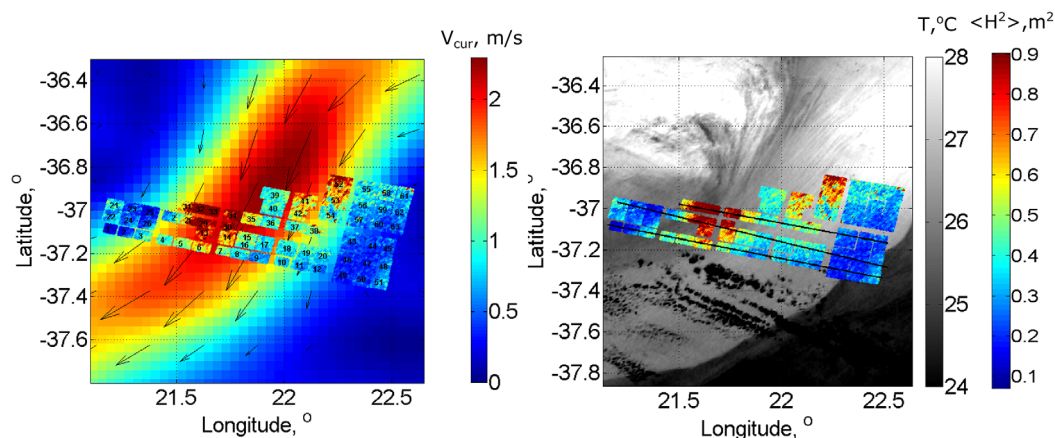


Figure 9. Set of selected Sentinel-2 MSI imagettes overlaid on (left) the altimeter geostrophic current, and (right) the SST field. Imagettes are color-coded according to the derived wave energy (surface variance, $\langle H^2 \rangle$) level. Each frame is numbered. Black lines on the right plot indicate transects discussed in the text. Contains modified Copernicus data (2016).

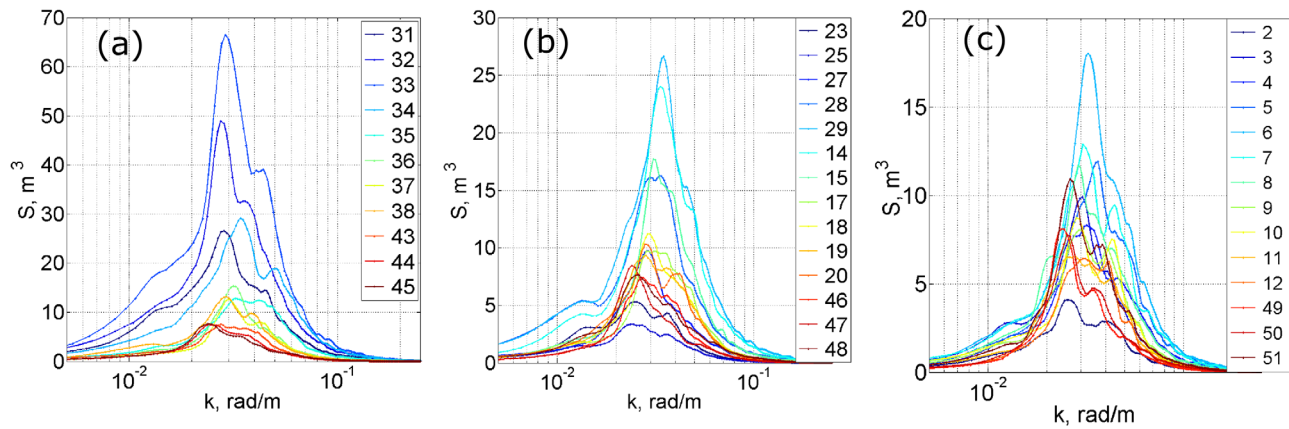


Figure 10. Omnidirectional wave spectra along (a) top, (b) middle, and (c) bottom transects indicated in Figure 9 (right). Color numbers corresponds to the frame indexed numbers in Figure 9.

Considering the set of Sentinel-2 MSI imageries intersecting the core of Agulhas current shown in Figure 9, it appears that the spatial variability of swell energy can be very strong across spatial distances of ~ 20 km and more. Referring to the altimeter-derived current map (Figure 9, left) swell energy strongly varies and generally increases within the current stream. The wave energy apparently decreases outside the current periphery. This is further illustrated in Figure 10. As found, the distribution of the omnidirectional wave spectra across the current exhibits drastic modulations. Changes in spectral levels can reach a factor 7 between values outside and inside the current. Unlike the spectral level, the spectral peak wave number

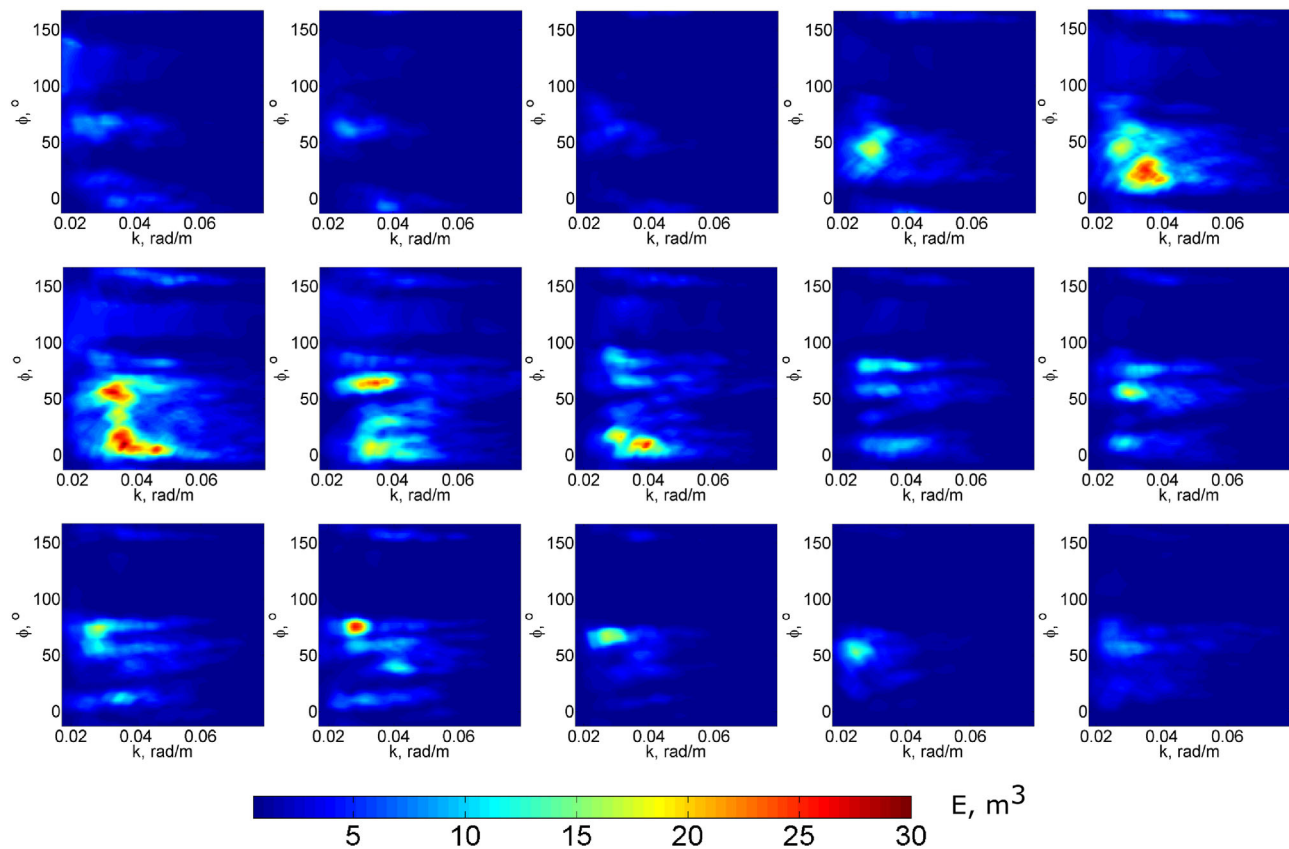


Figure 11. Evolution of the 2-D directional swell spectra along the middle transect, indicated in Figure 9 (right). From left-to-right and top-to-down corresponds to the evolution sequence from left-to-right, along the transect. Wave number vector directions are counted from the East, counterclockwise.

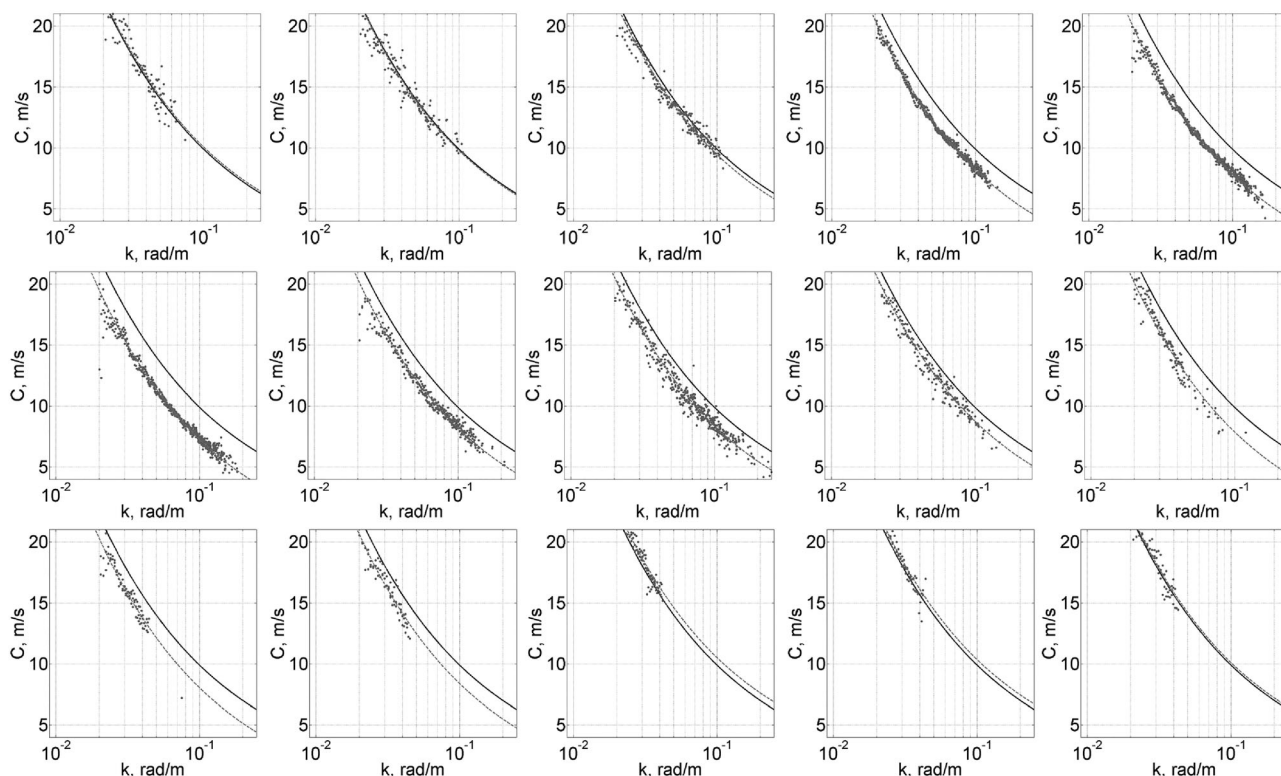


Figure 12. Phase shift between channels B04 (665 nm) and B08 (842 nm) expressed in terms of $c=c(k)$ compared to the linear dispersion relation: $c=(g/k)^{1/2}$, shown by black solid lines. Estimated deviations of measured $c(k)$ (symbols fitted by gray lines) from linear dispersion relation are treated as projection of the surface current on the wave direction. The plot sequence corresponds to Figure 11.

does not vary significantly across the current. However, a careful inspection of Figure 10 reveals that the increasing spectral level corresponds to increasing spectral peak wave number.

Figure 11 documents the surface wave transformation from their 2-D wave spectra along the middle transect shown in Figure 9 (right). For spectra outside the current, i.e., south of the current, corresponding to the three last spectra in the lowest row of Figure 11, a dominant wave mode is found, traveling in the 50–60° direction. Moving toward the current stream, corresponding to the two first spectra in the lowest row and the three last spectra in the middle row, an additional system emerges, traveling to the east (0°) direction. In the vicinity of the core of the current stream (corresponding to the two first spectra in the middle row and the last spectrum in the top row) these two wave systems are intensified, leading to an overall wave energy enhancement. North of the current, corresponding to the three first spectra in the top row, the spectral level drops. Yet, both wave systems still co-exist.

The evolution for the estimated dispersion relation can also be traced, as expressed in terms of phase velocity versus wave number, $c=c(k)$ and is shown in Figure 12. The local deviation of measured dispersion relation from the linear model, $c=(g/k)^{1/2}$, at given k corresponds to a projection of the surface current velocity on the wave direction (the Doppler shift). In our case, phase analysis is not yet sufficiently precise in order to retrieve the surface current vector using the velocity components derived from phase spectrum at different directions. Hence, the measured estimates of $c=c(k)$ shown in Figure 12 are the mean values obtained by averaging of the phase spectrum in a sector with angular width of 45°, which embraces the most energetic waves. Correspondingly, offset of observed $c=c(k)$ from the linear dispersion relation at given k , is a measure of the surface current. Referring to Figures 11 and 12, both the enhancement of wave spectral levels and the appearance of the additional wave system traveling eastward, correspond to noticeably large surface currents.

Profiles of the wave energy and estimated Doppler shift (surface current velocity), as well as integral parameters of the wave spectra along the three transects (as indicated in Figure 9) are presented in Figure 13. The

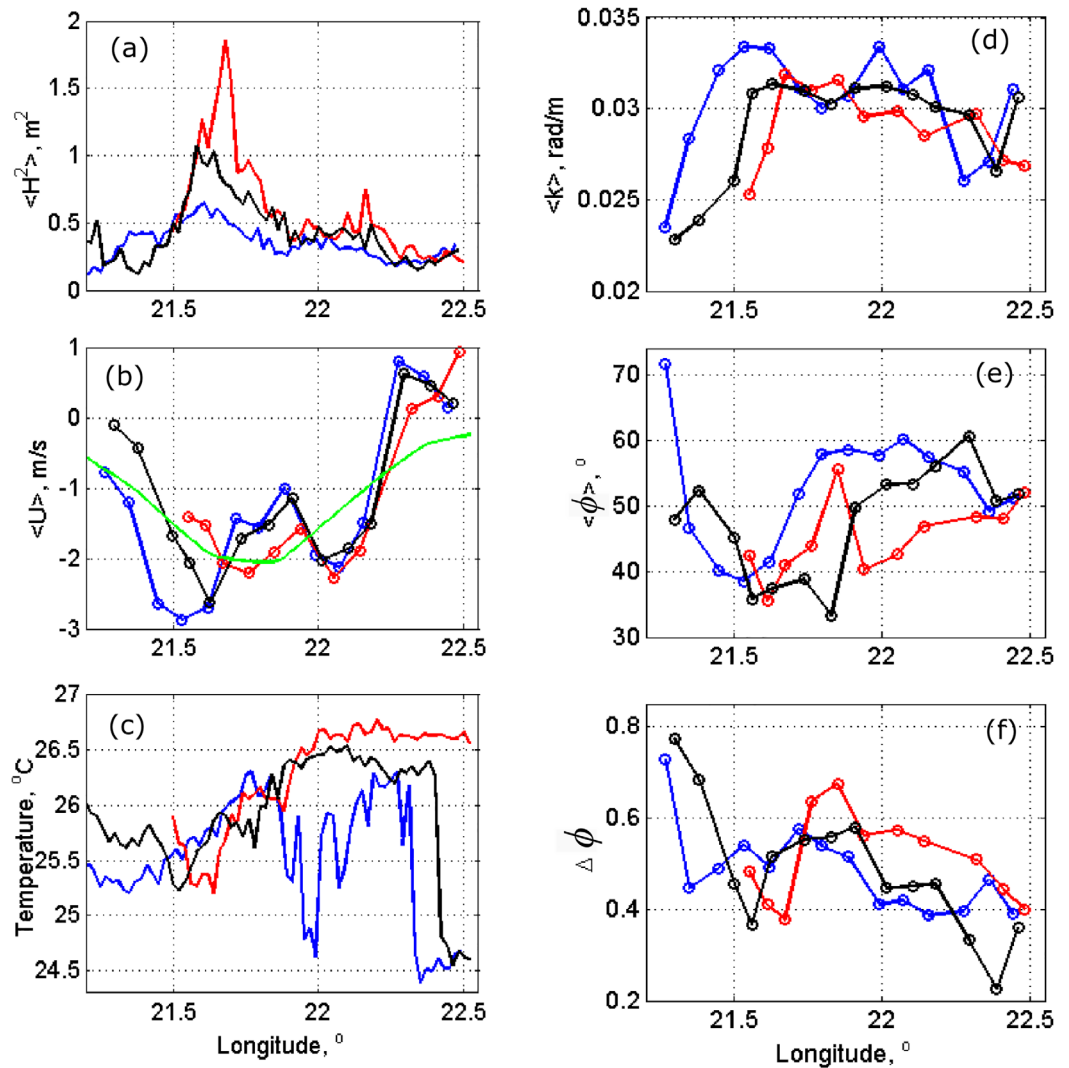


Figure 13. Left column: (a) wave energy profile, (b) surface current velocity derived from the estimated dispersion relation, and (c) SST. Right column: integral spectral parameters defined by (1), along the (red) top, (black) middle, and (blue) lower transects indicated in Figure 9 (right). Green line in Figure 13b is altimeter current velocity along middle transect.

integral spectral parameters, — mean wave number, \bar{K} , mean direction, $\bar{\phi}$, and angular width of the spectrum $\Delta\phi$, are defined via the spectral moments, $m_{\alpha\beta} = \int k_1^\alpha k_2^\beta S(\mathbf{k}) d\mathbf{k}$ [Longuet-Higgins, 1957]:

$$\begin{aligned} \bar{K} &= \frac{\sqrt{m_{10}^2 + m_{01}^2}}{m_{00}} \\ \tan(\bar{\phi}) &= \frac{m_{01}}{m_{10}} \\ \Delta\phi &= \left[\frac{m_{20} + m_{02} - \left((m_{20} - m_{02})^2 + 4m_{11}^2 \right)^{1/2}}{m_{20} + m_{02} + \left((m_{20} - m_{02})^2 + 4m_{11}^2 \right)^{1/2}} \right]^{1/2} \end{aligned} \tag{1}$$

Integration in (1) is performed over the wave number domain $1.7 \times 10^{-2} < k < 9 \times 10^{-2}$ rad/m. The energy of waves, shown Figure 13, is the variance of the reconstructed ocean surface elevation, and therefore has a higher spatial resolution than other quantities defined via spectral moments.

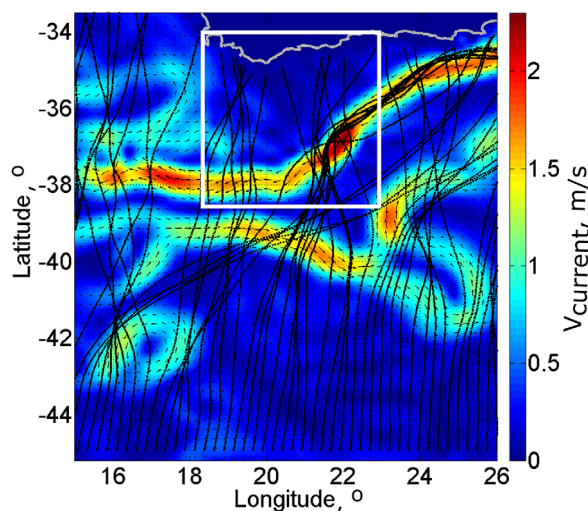


Figure 14. Wave-rays of an incoming 75° (counter clockwise from the East) swell at -45° latitude, with wave number $k=2.5 \times 10^{-2}$ rad/m. The altimeter surface current velocity field is taken from <http://www.aviso.altimetry.fr/en/data/products/sea-surface-height-products/global/madt-huv.html>. White box indicates area for Sentinel-2 data analysis.

Estimated surface current velocities, derived from Sentinel-2 MSI SSGI cross-channel analysis, provide consistent profiles over the Agulhas current. The wave energy is significantly enhanced on the northern side of the current jet. The amplification factor, the ratio between the maximum energy and swell energy south of the current, varies between transects and ranges from factor 2 to factor 7.

Mean wave numbers gradually increase from the southern boundary to the north but drop remarkably north of the current. To first order, this can be expected, as interaction of waves with opposite current should lead to shortening of wavelength by factor $(1-U/c_g)$. Yet, changes of the swell mean direction on the current seem to contradict this interpretation (northward deviation). This likely results from the emergence of a distinct additional swell system traveling eastward (recall Figure 11) forcing the mean

direction to also deviate eastwards, with an overall increase of the wave spectral direction spread (as seen in Figure 13).

These additional swell systems, traveling eastward, can be interpreted as surface waves trapped by the current, similarly to what was reported by Kudryavtsev *et al.* [1995]. Though the origin of the wave systems is different, wind-driven waves [Kudryavtsev *et al.*, 1995] and swell in the present study, the resulting effect of the surface wave interaction with opposing current is quantitatively very similar. In both cases, kinematic parameters of trapped waves (wave number and direction) are not too different from the parameters of the ambient waves, but the total energy of these waves significantly differs from the ambient level, due to the accumulation of refracted wave systems in the vicinity of the main current stream.

5. Model Simulations

After Snodgrass *et al.* [1966], more recent satellite SAR observations [Arduin *et al.*, 2009; Delpy *et al.*, 2010] confirm the weak dissipation of swell traveling over the oceans, with energy e-folding scales of about 3300 km. Recently, Badulin and Zakharov (S. Badulin and V. Zakharov, Ocean swell within the kinetic equation for water waves, submitted to *Nonlinear Processes in Geophysics*, 2016, doi:10.5194/npg-2016-61) investigated effect of nonlinear wave-wave interactions on swell evolutions, and found that their strong impact

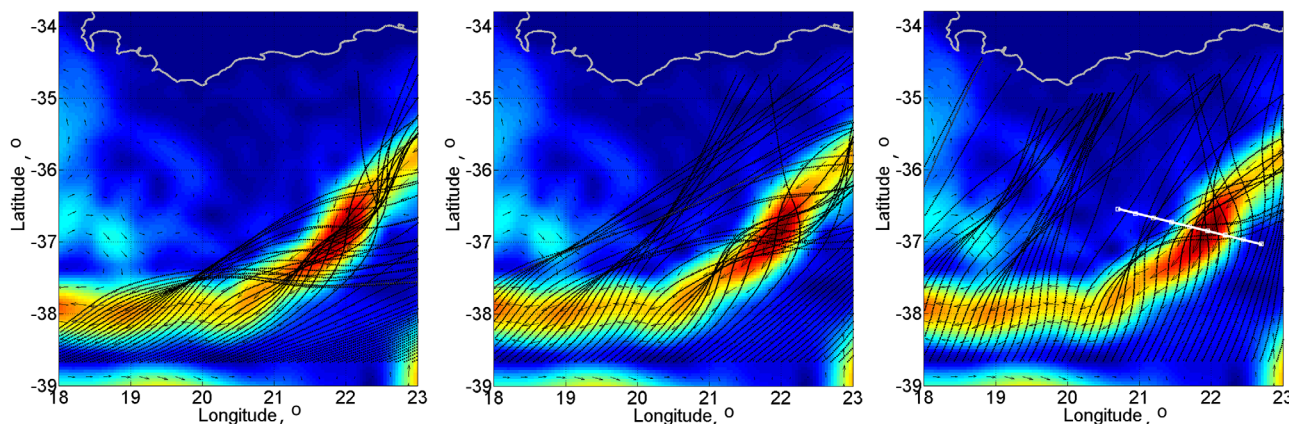


Figure 15. Swell-rays refracting on “local” surface current. Swell incidence angles are (left) 20°, (middle) 40°, and (right) 60° (counted counterclockwise from the East).

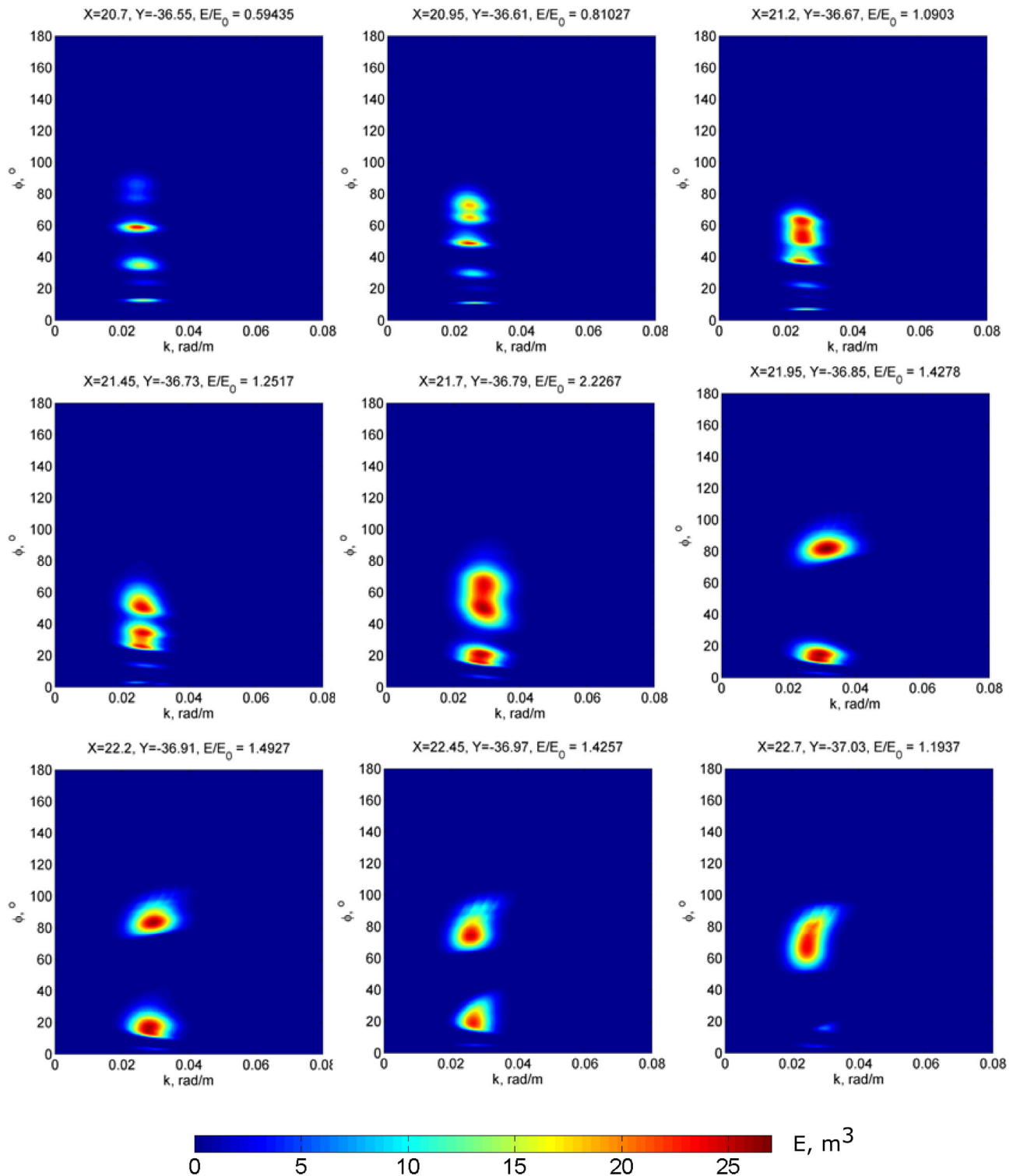


Figure 16. Simulated transformation of the swell spectra, along the middle transect shown Figure 15 (right). Top-left and bottom-right spectra correspond to left and right end of this transect. Incidence angle of swell is 60° , and angular width of the spectrum (δ) is $\Delta\phi = 15^\circ$.

exists only in “near field,”—on a distance of about hundred kilometres away from the swell “source.” Impact of wave-wave interactions on long term evolution of swell is rather weak leading to slow frequency downshift and energy attenuation (see Figure 10 from Badulin and Zakharov (submitted manuscript)). Considering swell evolution on the scales of the Agulhas current, we may thus ignore effect of swell dissipation and

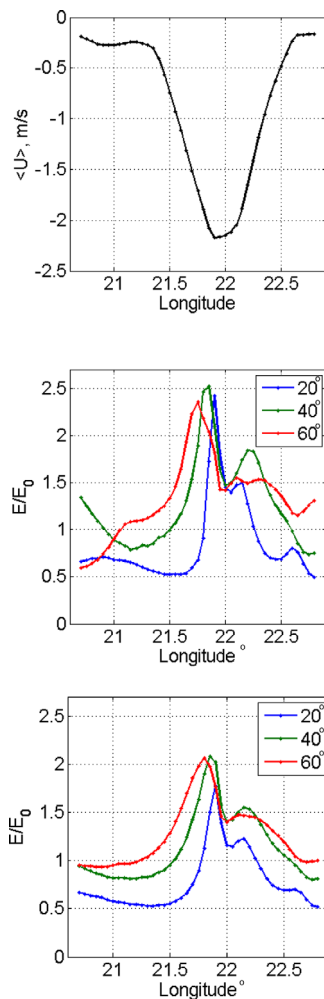


Figure 17. Profiles of (top) altimeter current velocity profile, and model wave energy scaled by initial value for (middle) narrow, $\Delta\phi = 15^\circ$, and (bottom) wide, $\Delta\phi = 30^\circ$, spectra along the transect shown in Figure 15 (right) at different swell incidence angles (color lines).

the midstream, and will then be solely guided by the current [see e.g., Kudryavtsev et al., 1995, for more detailed analysis of such a phenomenon].

To interpret the present observation, our analysis is further restricted to an area enclosing the Sentinel-2 MSI measurements shown in the white box marked on Figure 14. As already mentioned, swell systems have large relaxation scales, of order of thousands km, and a locally observed swell will maintain a “memory” of the previous multiple and remote interactions with surface currents encountered along the propagation from an initial remote source. Therefore, an ideal interpretation of observed swell features at a given ocean location must require model calculations of the wave transformation over a very large ocean area with specified surface currents (e.g., Gallet and Young, 2014). The latter are not always sufficiently well known. Accordingly and for the sake of simplicity, we hereafter focus on the effect of “local currents” on swell refraction. Local detected swell transformation will then be further combined, if necessary, with far zone remote cumulative transformations.

The 2-D energy spectrum of the incoming swell, $E_0(\mathbf{k})$, is taken in a form

$$E_0(\mathbf{k}) \propto \exp \left[- (k - k_p)^2 / \Delta k^2 - (\phi - \phi_p)^2 / \Delta \phi^2 \right] \quad (5)$$

wave-wave interactions. Following this assumption, the swell transformation follows ordinary differential equations describing the kinematics and dynamics of wave train evolution in the presence of surface currents [e.g., Phillips, 1977]:

$$\begin{aligned} dx_i / dt &= \partial \Omega / \partial k_i \\ dk_i / dt &= - \partial \Omega / \partial x_i \\ dN / dt &= 0 \end{aligned} \quad (2)$$

where $N(\mathbf{k}) = E(\mathbf{k}) / \omega$ is the wave action, $\omega = (gk)^{1/2}$ is the intrinsic frequency of the surface gravity waves on the deep water, and Ω is the dispersion function:

$$\Omega(\mathbf{k}, \mathbf{x}) = \omega(k) + k_j u_j \quad (3)$$

u_j is a component of the surface current velocity. The two first equations in (2) describe the evolution of wave rays and the wave train wave number along the modified trajectory. The third equation states the conservation of the wave action along the wave train evolution.

From the surface geostrophic current field derived from altimeter measurements, Figure 14 illustrates numerical solutions of the kinematic equations. Considering a quite long incoming swell, with wave number $k = 2.5 \times 10^{-2}$ rad/m, waves are traveling fast, with group velocity, c_g , about 10 m/s, and the ratio of current velocity u to c_g velocity is small $u/c_g \approx 0.2$. Nonetheless, remarkable scattering seems to be anticipated for an initial collinear field of incident swell rays. To recall, ray curvature arises from the local vorticity, $\text{Rot}(\mathbf{u})$, of the current [Kenyon, 1971]

$$r^{-1} = -c_g^{-1} \text{Rot}(\mathbf{u}) \quad (4)$$

and the cumulative impact of the current vorticity field on wave train kinematics can ultimately cause significant overall ray deflection (e.g., discussion by Munk et al. [2013] and Gallet and Young [2014]). Simulations performed by Rapizo et al. [2014] also illustrate the significant impact of Southern Ocean eddies on swell refraction. For the present case study, a spectacular convergence of swell rays, accumulated over the Agulhas stream core, is predicted, see top-right corner of Figure 14. The surface waves become trapped by the current. Following equation (4), the trajectory of wave trains traveling against the current shall then oscillate around

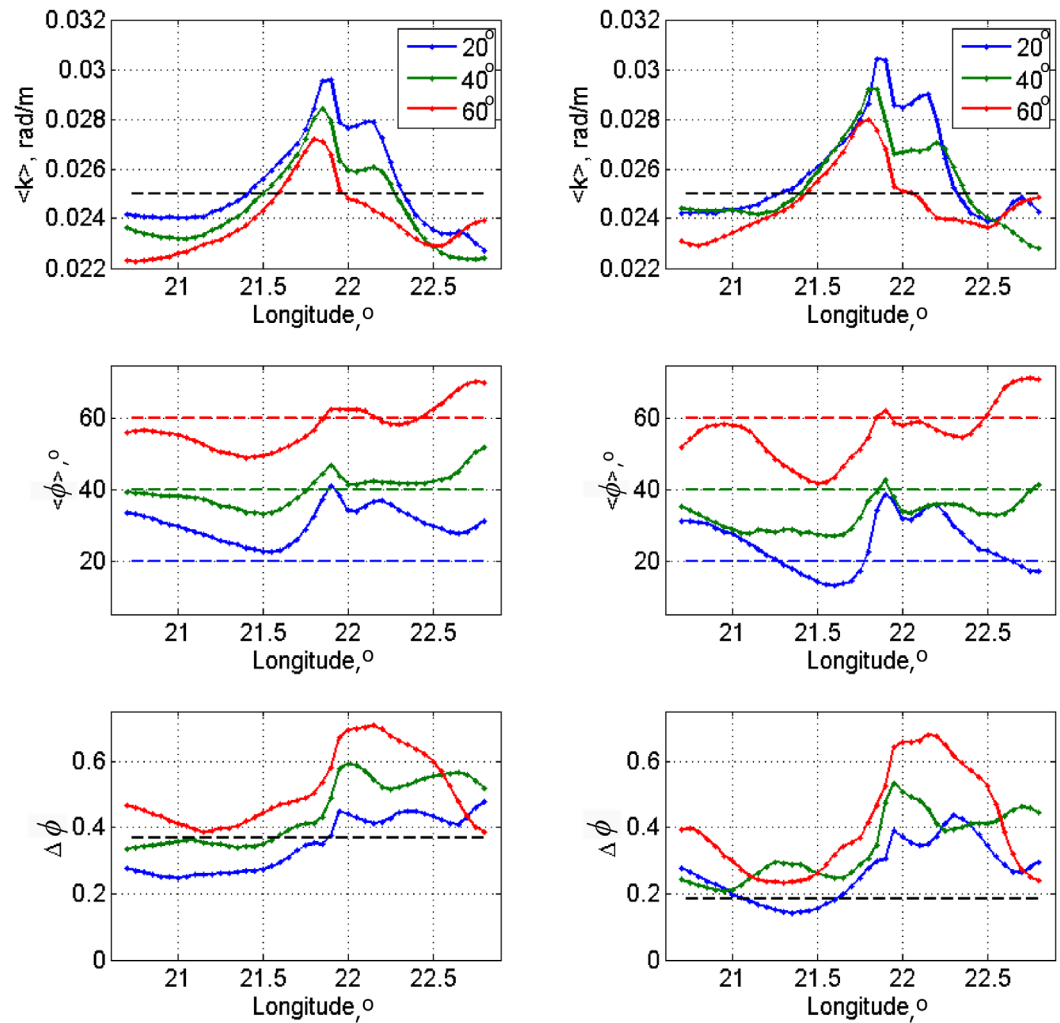


Figure 18. Profiles of the model integral spectral parameters defined by (1) along the transect shown in Figure 15 (right) for (left column) narrow, $\Delta\phi = 15^\circ$, and (right column) wide, $\Delta\phi = 30^\circ$, spectra for different swell incidence angles (color lines)

where k_p and ϕ_p are the spectral peak wave number and its direction, Δk and $\Delta\phi$ are the width of the spectrum in wave number and azimuth directions. We fix $\Delta k/k_p = 0.2$ and consider swell with “narrow”, $\Delta\phi = 15^\circ$, and “wide”, $\Delta\phi = 30^\circ$, directional spread. This initial spectrum enters the surface current area with three different incidence angles: 20° , 40° , and 60° , respectively.

The resulting trajectories are shown in Figure 15. For all cases, swell trains entering the current are subject to strong refraction. Near the Sentinel-2 MSI transects (recall Figure 9, right) a superposition of two wave systems is anticipated, in qualitative agreement with the observations of Figure 11.

To simulate the transformation of the swell spectrum, kinematic equations (equation (2) with equation (3)) are first solved at each given location. For each wave number, \mathbf{k} , forming the spectral grid at this given location, kinematic equations are integrated “back” to find the corresponding initial wave number value, \mathbf{k}_0 , at the boundary: $\mathbf{k}_0 = \mathbf{k}_0(\mathbf{k})$. As wave action is conserved along the wave trajectory, the swell energy spectrum at each given location follows:

$$E(\mathbf{k}) = E_0(\mathbf{k}_0(\mathbf{k})) \omega(\mathbf{k}) / \omega(\mathbf{k}_0(\mathbf{k})) \tag{6}$$

Simulated evolutions of swell spectra, along the white line transect indicated in the right-hand box of Figure 15, are shown in Figure 16 and appear qualitatively similar to observed spectra shown in Figure 11.

The swell energy is almost indifferent to initial incidence angles and spectral widths and is expected to increase inside the surface current regions as shown in Figure 17. In the core midstream area, the energy of

the swell system is amplified by factor 2–2.5. Compared to the energy of the swell near the current boundary, this amplification is 4–5. This amplification factor weakly depends on swell incidence angle and spectral width. In general, model estimates of swell energy modulations are consistent with the observations shown in Figure 13 and quantitatively reproduce the large swell energy enhancement within the core current area.

Compared with observed estimates shown in Figure 13, transformations of the integral spectral parameters, equation (1), are shown in Figure 18. Model simulations capture the evolution of the mean wave number of swell over the current, as well as the spectral directional broadening resulting from the superposition of refracted waves traveling in different directions.

6. Conclusion

In our Part 1 paper, a method is described to retrieve directional spectra of the surface wave elevations using satellite sun glitter imagery (SSGI). In this Part 2, the high-resolution space-time capability of large-swath Sentinel-2 MSI SSGI is further exploited to quantitatively map the transformation of the dominant surface waves, swell and wind-driven spectral peak waves, over the Great Agulhas current region. It is a known dangerous ocean area where giant (abnormally high) surface waves (swell) may suddenly appear [Mallory, 1974].

Sentinel-2 has been developed to address the requirements of the land monitoring applications within Copernicus. The Sentinel-2 imaging mode was thus not developed for the application discussed in this paper but rather to accommodate an extremely large-swath of 290 km while maintain a spatial resolution on ground of 10 m for land applications. This required that individual CCD detector arrays were positioned in a staggered manner to accommodate them on the focal plane of the MSI instrument. Overlaps between CCD arrays allow differences between detector arrays to be managed properly across the entire focal plane. As demonstrated, this configuration can be exploited to provide innovative new products, such as directional wave spectra and propagation characteristics, to help precisely quantify local changes in ocean wave energy and propagation direction.

Indeed, compared to high-altitude satellite SAR measurements, SSGI is not affected by wave motions that limit SAR imaging directional capabilities [e.g., Hasselmann *et al.*, 1985; Chapron *et al.*, 2001] to very long swell systems [Collard *et al.*, 2009], and provides a way to derive sea surface elevation statistics [e.g., Janssen and Alpers, 2006]. In such a context, the measurements from Sentinel-2 MSI shown here provide a novel and unambiguous view of oceanic sea states at small scales, to advance the understanding and modeling of ocean wind-wave-current interactions.

In this study, the Sentinel-2 MSI SSGI measurements are complemented by satellite altimeter measurements that collectively provide estimates of ocean geostrophic current and significant wave height. The altimeter-derived currents exhibit intense mesoscale variability with surface velocities reaching 2 m/s, in the Agulhas core current [e.g., Rouault *et al.*, 2010] that is also seen clearly in the corresponding sea surface temperature (SST) field. Our analysis of Sentinel-2 MSI SSGI, and further demonstrated using ray-tracing model calculations, mesoscale variability of the near-surface current can explain significant wave-current refraction, leading to both significant ray deflections and strong local enhancements of wave energy.

In particular, a significant enhancement of the wave energy is found in the main core surface current area that is also seen in SWH estimates from different altimeters. The current velocity profile estimated from the swell dispersion relation, derived from Sentinel-2 MSI cross-channel analysis, confirms that swell enhancement occurs in the core Agulhas stream and is shifted on the north edge (side) of the current. We find that the swell energy amplification factor, measuring the ratio between the wave energy inside and outside the current, varies from 3 to 7.

Spectra of incoming swell are unimodal, but inside the current, swell directional spectra broaden with the emergence of local wave components not aligned with the incoming swell. The measurements reveal a small increase of the mean swell wave number within the current, in accordance with expected shortening effect, by factor $(1 - u/c_g)$, for waves opposing the current. The emergence of additional wave components, coinciding with large enhancement of the energy (by a factor 3 to 7) is attributed to swell-trapping phenomenon. This is further confirmed using the ray-tracing model simulations. The strong currents can considerably refract the wave rays with direction and wave number changes, but also strongly modulate the

energy distribution by convergence and divergence of the rays. The current-induced variability thus creates gradients in wave heights that would be difficult to observe without high-resolution wide swath SSGI. The model simulations are capable to interpret these observations on a quantitative level, reproducing the similar transformation of 2-D swell spectra, and predicting the similar enhancement of swell energy associated to wave trapping.

In addition to their importance for wave modeling and hazard prediction, our results not only illustrate the overlooked potential of high-resolution sun glitter imagery, but also invite, to consider S2 measurements as unique opportunities to further assess and evaluate ocean products derived from Sentinel-1 A and B SAR measurements. Besides direct ocean wave spectra comparisons, S2 measurements can especially help to compare estimated Doppler shifts from S2 with Doppler residual information from S1 measurements, to more precisely evaluate and distinguish the wave-motion and surface current contributions [Chapron *et al.*, 2005].

Considering the wide-swath capability of Sentinel-2 observations, soon to be comforted with the future launch of Sentinel 2B, it certainly opens for new possibilities to combine actual and future satellite directional wave measurements (synthetic and real aperture radars) and altimeter observations to analyze short-range and long-range propagation of ocean swell systems to greatly improve the upper ocean mesoscale vorticity determination, as well as to derive more direct ocean surface currents from Space.

Acknowledgments

This work was supported through the ESA projects SARONG under contract 4000117644/16/NL/FF/gp and GlobCurrent under contract 4000109513/13/L-G, and the Russian Science Foundation grant 15-17-20020. The data used in this paper are available at: <https://scihub.copernicus.eu/dhus/#/home> (for Sentinel-2 data), <http://www.avisio.altimetry.fr/en/data/products/sea-surface-height-products/global/madt-h-uv.html> (for surface currents), <ftp://avisoftp.cnes.fr/AVISOPub> (for Jason-2 and Saral tracks on 3–5 January 2016), and at ftp://podaac-www.jpl.nasa.gov/OceanTemperature/ghrsst/data/GDS2/L2P/VIIRS_NPP/OSPO/v2.4/2016/004/20160104122000-OSPO-L2P_GHRSSST-SSTskin-VIIRS_NPP-ACSPO_V2.40-v02.0-fv01.0.nc (for SST on 4 January 2016, 12:20 GMT). The authors are grateful to two anonymous Reviewers for their useful comments.

References

- Ardhuin, F., B. Chapron, and F. Collard (2009), Observation of swell dissipation across oceans, *Geophys. Res. Lett.*, *36*, L06607, doi:10.1029/2008GL037030.
- Barnett, T. P., F. Keller, and B. Holt (1989), Estimation of the two-dimensional ocean current shear field with a synthetic aperture radar, *J. Geophys. Res.*, *94*(C11), 16,087–16,095.
- Beal, R., V. Kudryavtsev, D. Thompson, S. Grodsky, D. Tilley, V. Dulov, and H. Graber (1997), The influence of the marine atmospheric boundary layer on ERS-1 synthetic aperture radar imagery of the Gulf Stream, *J. Geophys. Res.*, *102*(C3), 5799–5814.
- Chapron, B., H. Johnsen, and R. Garello (2001), Wave and wind retrieval from SAR images of the ocean, *Ann. Telecommun.*, *56*, 682–699.
- Chapron, B., F. Collard, and F. Ardhuin (2005), Direct measurements of ocean surface velocity from space: Interpretation and validation, *J. Geophys. Res.*, *110*, C07008, doi:10.1029/2004JC002809.
- Collard, F., F. Ardhuin, and B. Chapron (2009), Monitoring and analysis of ocean swell fields from space: New methods for routine observations, *J. Geophys. Res.*, *114*, C07023, doi:10.1029/2008JC005215.
- Delpey, M. T., F. Ardhuin, F. Collard, and B. Chapron (2010), Space-time structure of long ocean swell fields, *J. Geophys. Res.*, *115*, C12037, doi:10.1029/2009JC005885.
- Gallet, B., and W. R. Young (2014), Refraction of swell by surface currents, *J. Mar. Res.*, *72*(2), 105–125.
- Gutshabash, Ye.Sh., and L. V. Lavrenov (1986), Swell transformation on current at the Igolny Cape [in Russian], *Izvestiya Acad. Sc. USSR, FAO*, *22*(6), 526–531.
- Hasselmann, K., R. K. Raney, W. J. Plant, W. Alpers, R. A. Shuchman, D. R. Lyzenga, C. L. Rufenach, and M. J. Tucker (1985), Theory of synthetic aperture radar ocean imaging: A MARSEN view, *J. Geophys. Res.*, *90*(C3), 4659–4686.
- Irvine, D., and D. G. Tilley (1988), Ocean wave directional spectra and wave-current interaction in the Agulhas from the Shuttle Imaging Radar-B synthetic aperture radar, *J. Geophys. Res.*, *93*(C12), 15,389–15,401.
- Janssen, P., and W. Alpers (2006), Why SAR wave mode data of ERS and Envisat are inadequate for giving the probability of occurrence of freak waves, in *Proceedings of the SEASAR 2006 Workshop (Advances in SAR Oceanography from Envisat and ERS Missions)*, edited by H. Lacoste and L. Ouwehand, ESA SP-613, ESA/ESRIN, Frascati, Italy.
- Kenyon, K. E. (1971), Wave refraction in ocean currents, *Deep Sea Res. Oceanogr. Abstr.*, *18*, 1023–1034.
- Kozlov, I., V. Kudryavtsev, J. Johannessen, B. Chapron, I. Dailidiene, and A. Myasoedov (2012), ASAR imaging for coastal upwelling in the Baltic Sea, *J. Adv. Space Res.*, *50*, 1125–1137, doi:10.1016/j.asr.2011.08.017.
- Kudryavtsev, V. N., and A. V. Soloviev (1990), Slippery near-surface layer of the ocean arising due to daytime solar heating, *J. Phys. Oceanogr.*, *20*, 617–628.
- Kudryavtsev, V. N., S. A. Grodsky, V. A. Dulov, and A. N. Bol'shakov (1995), Observations of wind waves in the Gulf Stream frontal zone, *J. Geophys. Res.*, *100*(C10), 20,715–20,728.
- Kudryavtsev, V. N., S. Grodsky, V. Dulov, and V. Malinovsky (1996), Observation of atmospheric boundary layer evolution above the Gulf Stream frontal zone, *Boundary Layer Meteorol.*, *79*, 18–82.
- Kudryavtsev, V., D. Akimov, J. Johannessen, and B. Chapron (2005), On radar imaging of current features, Part 1: Model and comparison with observations, *J. Geophys. Res.*, *110*, C07016, doi:10.1029/2004JC002505.
- Kudryavtsev, V., A. Myasoedov, B. Chapron, J. Johannessen, and F. Collard (2012), Imaging meso-scale upper ocean dynamics using SAR and optical data, *J. Geophys. Res.*, *117*, C04029, doi:10.1029/2011JC007492.
- Lavrenov, I. V. (2003), *Wind-Waves in Oceans: Dynamics and Numerical Simulations*, 376 pp., Springer, Berlin.
- Liu, A. K., C. Y. Peng, and J. D. Schumacher (1994), Wave-current interaction study in the Gulf of Alaska for detection of eddies by synthetic aperture radar, *J. Geophys. Res.*, *99*(C5), 10,075–10,085.
- Longuet-Higgins, M. S. (1957), Statistical analysis of random moving surface, *Philos. Trans. R. Soc. London*, *249*(966), 321–360.
- Mallory, J. K. (1974), Abnormal waves on the south-east of South Africa, *Inst. Hydrogen Rev.*, *51*, 89–129.
- Mapp, G. R., C. S. Welch, and J. C. Munday (1985), Wave refraction by warm core rings, *J. Geophys. Res.*, *90*(C4), 7153–7163.
- McLeish, W., and D. B. Ross (1985), Wave refraction in an ocean front, *J. Geophys. Res.*, *90*(C6), 11,929–11,938.
- Meadows, G. A., R. A. Schuman, Y. C. Tseng, and E. S. Kasichke (1983), Seasat synthetic aperture radar observations of wave-current and wave-topographic interactions, *J. Geophys. Res.*, *88*(C7), 4393–4406.

- Munk, W., G. Millet, F. Snodgrass, and N. Barber (2013), Correction: Direction recording of swell from distant storms, *Philos. Trans. R. Soc. A*, 255, 505–584, doi:10.1098/rsta.2013.0039.
- Phillips, O. M. (1977), *The Dynamics of the Upper Ocean*, 2nd ed., Cambridge Univ. Press, New York.
- Rapizo, H, A. V. Babanin, O. Gramstad and M. Ghantous (2014), Wave refraction on Southern Ocean Eddies, *19th Australasian Fluid Mechanics Conference*, Melbourne, Australia, 8–11 December.
- Rascle, N., B. Chapron, A. Ponte, F. Ardhuin, and P. Klein (2014), Surface roughness imaging of currents shows divergence and strain in the wind direction, *J. Phys. Oceanogr.*, 44, 2153–2163, doi:10.1175/JPO-D-13-0278.1.
- Rouault, M. J., A. Mouche, F. Collard, J. A. Johannessen, and B. Chapron (2010), Mapping the Agulhas Current from space: An assessment of ASAR surface current velocities, *J. Geophys. Res.*, 115, C10026, doi:10.1029/2009JC006050.
- Snodgrass, F. E., G. W. Groves, K. Hasselmann, G. R. Miller, W. H. Munk, and W. H. Powers (1966), Propagation of ocean swell across the Pacific, *Philos. Trans. R. Soc. London A*, 249, 431–497.
- Stuart-Menteth, A. C., I. S. Robinson, R. A. Weller, and C. J. Donlon (2005), Sensitivity of the diurnal warm layer to meteorological fluctuations. Part 1: Observations, *J. Atmos. Ocean Sci.*, 10(3), 193–208.